

Cite this: *J. Mater. Chem. A*, 2018, 6, 23435

Controlled synthesis of Pt nanoparticle supported TiO₂ nanorods as efficient and stable electrocatalysts for the oxygen reduction reaction†

Paskalis Sahaya Murphin Kumar,^a Vinoth Kumar Ponnusamy,^{cd} Koolath Ramakrishnan Deepthi,^a Gopalakrishnan Kumar,^e Arivalagan Pugazhendhi,^f Hideki Abe,^g Sivakumar Thiripuranthagan,^{*b} Umapada Pal,^g and Siva Kumar Krishnan^{id} ^{*h}

The development of adequate cathode materials is one of the principal tasks for the fabrication of efficient proton-exchange membrane fuel cells (PEMFCs), which are envisaged as clean energy sources for future transport and portable electrodomestic applications. Here, we present a platinum nanoparticle (NPs)-decorated one-dimensional (1D) titanium dioxide nanorod (PtNPs/TiO₂NRs) nanocomposite with enhanced electrocatalytic performance towards the oxygen reduction reaction (ORR). The TiO₂NRs were prepared through a green approach, utilizing seaweed extract that not only acts as a reducing agent but also serves as a soft template for the directional growth of TiO₂ nanostructures. PtNPs of about 3.0 nm average size were decorated over pre-synthesized TiO₂NRs through the chemical reduction of Pt ions using sodium borohydride. Scanning electron microscopy (SEM), transmission electron microscopy (TEM), X-ray diffraction (XRD), X-ray photoelectron spectroscopy (XPS), and Raman spectroscopy analyses confirmed the presence of strong metal-support interactions (SMSI) in the prepared hybrid nanocomposite. The as-prepared PtNPs/TiO₂NRs composite nanostructures exhibited significantly enhanced electrocatalytic performance and stability towards the ORR, with specific and mass activities of 0.428 mA cm⁻² at 0.55 V and 128 mA mg⁻¹ Pt, respectively. These values are 7.2 and 3.5 fold higher than that of standard Pt/C catalysts (0.059 mA cm⁻² and 36 mA mg⁻¹ Pt), respectively. The enhanced catalytic activity and high stability of the composite catalyst are mainly due to the unique 1D morphology of the TiO₂ nanostructures, which provides a greater surface area, and the SMSI enhancing electron transfer rate at their functional interface. The green approach utilized to fabricate the Pt/TiO₂NRs composite in the present study provides a new, low-cost strategy for the development of metal-oxide hybrid nanostructures of high electrocatalytic activity for fuel cell applications.

Received 30th July 2018
Accepted 25th October 2018

DOI: 10.1039/c8ta07380e

rsc.li/materials-a

Introduction

Proton-exchange membrane fuel cells (PEMFCs) are considered as the most valuable components of efficient, clean, and sustainable energy conversion systems, owing to their high power density, high reliability, and low carbon emission.¹ Nanostructured platinum (Pt) plays an indispensable role as

a most active metal electrocatalyst, which has been ubiquitously utilized for the efficient and durable oxygen reduction reaction (ORR) at the cathodes of PEMFCs with tunable activity and high selectivity.^{2,3} However, the high cost and low utilization efficiency or lifetime of Pt-based cathodes are the principal limitations, impeding the commercialization of PEMFCs at the industrial scale.⁴ Therefore, finding new, efficient, and cost-

^aNational Institute for Materials Science (NIMS), 1-1 Namiki, Ibaraki Tsukuba, 305-0044 Japan^bDepartment of Applied Science and Technology, Anna University, Chennai, Tamil Nadu 600-025, India. E-mail: sivakumar@annauniv.edu^cResearch Centre for Environmental Medicine, Kaohsiung Medical University, Kaohsiung City, Taiwan^dDepartment of Medicinal and Applied Chemistry, Kaohsiung Medical University, Kaohsiung City, Taiwan^eInstitute of Chemistry, Bioscience and Environmental Engineering, Faculty of Science and Technology, University of Stavanger, Box 8600 Forus, 4036 Stavanger, Norway^fFaculty of Environment and Labour Safety, Ton Duc Thang University, Ho Chi Minh City 756600, Vietnam^gInstituto de Física, Benemérita Universidad Autónoma de Puebla, Apdo. Postal J-48, Puebla 72570, Mexico^hCONACYT – Instituto de Física, Benemérita Universidad Autónoma de Puebla, Apdo. Postal J-48, Puebla 72570, Mexico. E-mail: sivakumar@ifuap.buap.mx† Electronic supplementary information (ESI) available: Particle size distribution histogram, EDS-analysis, LSV curves and Tafel plots of the Pt/TiO₂NRs, Pt/Comm. TiO₂ and Pt/C catalysts, CO-stripping analysis, TEM and XPS results of the catalyst after ADT. See DOI: 10.1039/c8ta07380e

effective materials as the replacements for Pt is the current challenge. Substantial research has been directed towards the preparation of Pt-supported catalysts, which not only reduce the use of Pt but are also efficient electrocatalysts for the ORR.^{5,6} One of the most successful strategies is the incorporation of PtNPs over metal oxide supports,^{7,8} exploiting the synergetic effect of strong metal-support interactions (SMSI),⁹ which often exquisitely enhance the electrocatalytic performance of PtNPs and the durability of the catalysts. However, the efficiency of a Pt-supported metal oxide electrocatalyst relies greatly on the size and morphology of the metal NPs,¹⁰ the interaction between the metal and oxide support,¹¹ and the surface segregation dynamics of the supported NPs.¹²

Recently, vast research efforts have been devoted to fabricating Pt-supported hybrid systems, including Pt/TiO₂,^{13,14} Pt/Ti_xMO_xO₂,¹⁵ Pt/CeO₂,^{16,17} Pt/SiO₂,¹⁸ Pt/MnO₂,¹⁹ Pd/WO_x,²⁰ and Pt/SnO_x (ref. 21) as alternatives to the conventional bare Pt nanostructures, with substantially improved electrocatalytic activity and stability. The SMSI primarily occur *via* bond formation between the supported metal and the oxygen vacancy sites of the oxide support.²² Among the various metal oxide supports studied so far, TiO₂ nanostructures seem to be the most attractive candidates due to their unique electronic structures, high stability in acidic environments, and high defect contents, which enable strong interactions between the metal nanoparticles and TiO₂ support.^{23–25} High corrosion resistance under alkaline conditions, low cost, low toxicity, and high abundance of TiO₂ are some added advantages for utilizing their nanostructures as catalysts in the ORR.^{14,26} Furthermore, the controlled synthesis and assembly of one-dimensional (1D) TiO₂NRs decorated by PtNPs have drawn particular interest due to their remarkably enhanced electronic conductivity, high photocatalytic activity,²⁷ and excellent electrocatalytic performances.^{11,14} Numerous synthetic approaches such as hydrothermal,²⁸ sol-gel,²⁹ microwave-assisted growth,³⁰ and wet-chemical synthesis³¹ have been utilized for the fabrication of TiO₂NRs. However, with most of these approaches, there is a struggle to obtain nanostructures of the desired size, shape and orientation. From this perspective, the development of a green, eco-friendly synthetic approach for the fabrication of TiO₂ nanostructures in a controlled manner at low cost, such as biosynthesis, is presently of immense scientific and technological interest.³² Macroalgae polymers extracted from seaweed have numerous side groups, which provide a new synthetic platform, enabling the controlled synthesis of metal/metal oxide nanostructures of well-defined morphologies, with excellent performance in a wide range of applications.^{33,34}

In the present work, we describe a green strategy for the controlled fabrication of 1D TiO₂NRs using a macroalgae polymer extracted from seaweed, which not only serves as a mild reducing agent but also acts as a template for the directional growth of TiO₂. The TiO₂NRs were decorated with PtNPs of *ca.* 3.0 nm average size, and the composite catalysts were tested for the ORR. The Pt/TiO₂NRs hybrid nanostructures displayed high electrocatalytic efficiency and long-term durability towards the

ORR in alkaline conditions, superior to the state-of-the-art Pt/C and Pt/TiO₂ catalysts fabricated with commercial TiO₂ nanostructures (Pt/TiO₂(Comm)).

Experimental

Materials and methods

Titanium (IV) isopropoxide Ti[OCH(CH₃)₂]₄, 99.9%), chloroplatinic acid hexahydrate (H₂PtCl₄·6H₂O, 99.98%), sodium borohydride (NaBH₄, >99.9%), titanium dioxide nanopowder (particle size < 22 nm, anatase > 95%), and commercial Pt/C (20 wt%) catalysts were purchased from Sigma-Aldrich (USA). All the chemicals were utilized as received, without further purification. All the glassware were washed with deionized (DI) water and air-dried before use.

Preparation of the seaweed extract

The brown colored seaweeds (*Turbinaria conoides*) were collected from the southeast coast of India (Mandapam coastal region, 78°8'E, 9°17'N). They were first washed thoroughly with tap water, and then with distilled water in order to eliminate the adhered salts and biota. Then, the samples were dried under ambient conditions for a week. The dried seaweed sample was ground in a conventional mixer grinder to obtain a fine powder. To obtain the aqueous extract, 5 g of the seaweed powder was dispersed in 100 mL of DI water under ultrasonication for 1 h and then boiled at 100 °C for 20 min. After cooling down to room temperature, the solution was filtered to collect the aqueous extract.

Seaweed extract-assisted green synthesis of TiO₂ nanorods

For the synthesis of the TiO₂NRs, 10 mL of the seaweed extract was mixed with 90 mL of 1 mM aqueous titanium isopropoxide solution (prepared under ice bath) under constant magnetic stirring until the color of the reaction solution turned light green. The green color of the solution indicated the formation of TiO₂NRs. The formed nanostructures were separated from the solution by centrifuging at 10 000 rpm for 15 min, washed with DI water for four times, filtered, and then allowed to dry at 80 °C for 12 h.

Synthesis of Pt/TiO₂NRs hybrid structures

The hybrid Pt/TiO₂NRs sample was obtained by a facile seed-mediated chemical reduction strategy, using TiO₂NRs as the seed and NaBH₄ as the reducing agent. In a typical synthesis, 50 mL of DI water containing 50 mg of pre-synthesized TiO₂NRs was mixed with 10 mL of aqueous Pt precursor solution (5 mM) and kept under magnetic stirring for 1 h. Then, 0.5 mL of freshly prepared aqueous NaBH₄ solution (0.1 M) was slowly added to the mixture to reduce the Pt ions over TiO₂NRs. The mixture was kept under magnetic agitation for another 30 min. We optimized the concentration of NaBH₄ to obtain smaller PtNPs without agglomeration over the TiO₂NRs support. The final product was washed four times using DI water in order to eliminate the un-impregnated PtNPs and dried overnight in an oven at 60 °C. The PtNPs were also supported over commercial TiO₂NPs using the same protocol (using optimized conditions) and the obtained composite was designated as Pt/TiO₂(Comm).

Characterization of materials

The morphologies of the fabricated nanostructures were inspected using a Hitachi SU8230 scanning electron microscope (SEM) operated at 15 kV accelerating voltage. Transmission electron microscopy (TEM) and high-resolution TEM (HR-TEM) images of the samples were acquired in a JEOL 2100-F2 microscope operated at 200 kV. For elemental analysis and elemental mapping, a JED-2300T JEOL energy-dispersive spectrometer (EDS) was utilized. For TEM and EDS-mapping analyses, the samples were first dispersed in ethanol under ultrasonication for 15 min. Then, a drop of the suspension was spread over a carbon-coated copper (Cu) grid, and dried overnight at room temperature. The powder X-ray diffraction (XRD) patterns of the samples were obtained in an EXPERT-PRO, PANalytical diffractometer, utilizing monochromatic Cu K α radiation ($\lambda = 0.15406$ nm) in the 20–100 degree 2θ range, in 0.025 degree steps. Room temperature Raman spectra of the samples were recorded in a Jasco NRS-3100 Raman spectrometer. For Raman analysis, the samples were deposited over silicon wafers and excited with a 632.8 nm He–Ne laser source of 0.025 mW power. The UV-vis absorption spectra of the samples were recorded in a UV-vis spectrophotometer (V-7200, JASCO, NIMS, Japan) in the 250–800 nm spectral range. Room temperature photoluminescence (PL) spectra of the samples were recorded in an assembled set-up, utilizing the 325 nm emission of a He–Cd laser as the excitation source. N $_2$ adsorption–desorption isotherms of the samples were measured in a Micrometrics ASAP 2020 system after degassing them at 150 °C for 3 h. For X-ray photoelectron spectroscopy (XPS) analysis of the samples, a PHI Quantera SXM, ULVAC-PHI system containing an Al K α X-ray source (1.4×0.1 mm, 100 W, 20 kV, 5 mA) was utilized.

Electrochemical measurements

The cyclic voltammetry (CV) studies of the electrocatalysts were performed using a conventional three-electrode electrochemical workstation (cell volume: 100 mL, PINE Co.), with glassy carbon (GC) as the rotating disk electrode (RDE, 5 mm diameter), and Pt foil and a Ag/AgCl electrode (4 M KCl) as the counter electrode and reference electrode, respectively. The working electrode was fabricated as follows. The catalytic ink was prepared by mixing 4.0 mg of the Pt/TiO $_2$ NRs or Pt/TiO $_2$ (Comm) sample with 4.0 mg of carbon black (Vulcan XC 72), 1.75 mL of DI water, 440 μ L of isopropyl alcohol, and 20 μ L of liquid Nafion (5% solution, EW: 1100, Aldrich) under ultrasonication, obtaining a well-dispersed suspension. Finally, 45 μ L of the above suspension was drop-casted onto the cleaned GC electrode and then allowed to dry under ambient conditions. The Pt loading onto the GC electrode was 15 μ g cm $^{-2}$. The Pt/C (20 wt%) electrode was prepared in a similar way, using the commercial Pt/C catalyst.

The cyclic voltammetry (CV) measurements were carried out in Ar- or O $_2$ -saturated 0.1 M HClO $_4$ solution over a potential range of -0.2 to $+1$ V *versus* vs. Ag/AgCl at a scan rate of 20 mV s $^{-1}$. The electrochemical surface area (ECSA) was estimated by integrating the hydrogen under-potential charge in the

adsorption/desorption region of the CV curves in an Ar-saturated atmosphere in the potential range of -0.18 to $+0.20$ V $_{RHE}$, with a reference value of 210 μ C cm $^{-2}$ for a monolayer of adsorbed hydrogen on the Pt surface divided by the Pt mass loaded on the working electrode. The ORR polarization curves of the catalysts were recorded in the RDE system (PINE instrumentation) in an O $_2$ -saturated 0.1 M HClO $_4$ solution at the scan rate of 2 mV s $^{-1}$ and rotating speed ranging from 400 to 2000 rpm. The kinetic current (I_k) from the positive on-going ORR polarization curves was calculated using the well-known Koutecky–Levich (KL) equation:³⁵

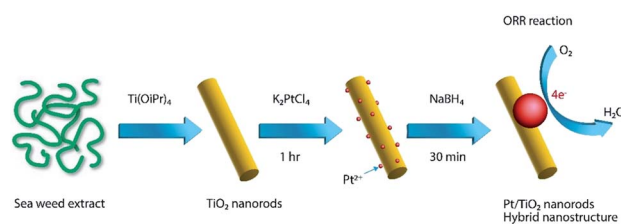
$$\frac{1}{I} = \frac{1}{I_k} + \frac{1}{I_d} \quad (1)$$

where I is the measured current density, I_k is the kinetic-limiting current density, and I_d is the diffusion-limiting current density. The specific and mass activities of the electrocatalysts were estimated from their ORR polarization curves by normalizing I_k to the corresponding electrochemical surface area (ECSA), and the mass of Pt in the active electrodes, respectively. The durability of the electrocatalysts was tested using accelerated durability tests (ADTs) in an Ar-saturated aqueous 0.1 M HClO $_4$ solution over a potential range of $+0.5$ to $+1.0$ V at a scan rate of 20 mV s $^{-1}$ after 10 000 continuous scanning cycles.

Results and discussion

Synthesis and structural characterization of Pt/TiO $_2$ NRs

Fabrication of the Pt/TiO $_2$ NRs hybrid nanostructures involved two steps, namely, synthesis of TiO $_2$ NRs using seaweed extract, and incorporation of PtNPs over TiO $_2$ NRs. The seaweed contains macroalgae polymer, which serves as a template as well as a mild reducing agent for the controlled 1D growth of TiO $_2$ NRs. Moreover, the macroalgae polymers possess numerous functional groups that can act as mild reducing and stabilizing agents to obtain metallic and metal oxide nanostructures with well-controlled sizes and shapes.^{33,34} Previous studies provided evidence that the side groups of those polymers such as hydroxyl (–OH) ions serve as mild reducing agents for metal ions, generating metal NPs.³⁶ Scheme 1 illustrates the steps involved in the preparation of Pt/TiO $_2$ NRs hybrid nanostructures. Briefly, the TiO $_2$ NRs were obtained through seaweed-assisted slow reduction of Ti precursor, leading to slow nucleation and growth processes. Such slow nucleation and



Scheme 1 Schematic representation of the seaweed-mediated synthesis process of TiO $_2$ NRs, followed by the formation of PtNPs over TiO $_2$ NRs using a chemical reduction process.

growth processes lead to the growth of 1D TiO₂ structures in a controlled manner between the polymeric chains, resulting in the formation of TiO₂NRs with controlled diameter. In the second step, small uniformly dispersed PtNPs were formed over TiO₂NRs through the seed-mediated growth process. The pre-synthesized TiO₂NRs were used as seeds to reduce Pt ions over them using NaBH₄, which is a strong reducing agent (Scheme 1).³⁷

The morphology of the pristine TiO₂NRs sample was monitored by scanning electron microscopy (SEM). As shown in Fig. 1, the obtained pristine TiO₂NRs have a rod-like morphology. While some of these structures are long enough to be considered nanowires, a few of them are quite short in length. For simplicity, they are collectively denoted as TiO₂NRs in this article. The diameters of the formed nanorods varied between 25 and 60 nm and their length varied from 100 to 300 nm (ESI, Fig. S1†). A close observation of the high magnification image presented in Fig. 1b reveals that the nanorods form a densely assembled chain-like structure. The side-by-side assembly of the TiO₂NRs is probably due to the strong electronic interactions and the presence of oxygen vacancies at their surface. The formation of similar assemblies has also been reported for WO_xNRs and is attributed to the strong electronic interactions.^{20,38}

The formation of Pt/TiO₂NRs hybrid structures was examined by transmission electron microscopy (TEM). The images presented in Fig. 2 a, b, clearly indicate the formation of well-dispersed Pt particles over TiO₂NRs. The formed PtNPs appear as darker spots over the TiO₂NRs. The HR-TEM image presented in Fig. 2c demonstrates the formation of well-crystalline Pt particles, strongly coupled with the surface of TiO₂NRs. The interplanar spacing *d* estimated from the HR-TEM image of Pt nanoparticle was 0.2248 nm (inset in Fig. 2c), matching the interplanar distance of the (111) planes of the face-centered cubic (fcc) metallic PtNPs.^{15,39} The size distribution histogram of the Pt particles (Fig. 2d) revealed an average nanoparticle size of 3 ± 1 nm with a narrow size distribution.

The distribution of PtNPs in the Pt/TiO₂NRs was studied further using EDS elemental mapping. Fig. 3 shows a typical HAADF-STEM image and corresponding EDS-elemental mapping images of the composite, revealing the uniform distribution of Pt (yellow) over the TiO₂NRs (red and green). The Pt-enriched surface of the composite nanostructures is very clear in the overlay image presented in Fig. 3. A closer

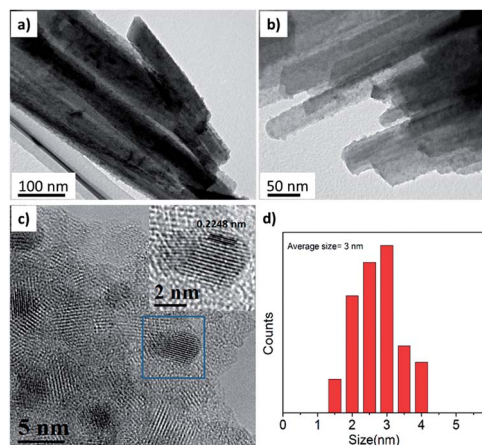


Fig. 2 (a) Low, and (b) high-magnification TEM images of Pt/TiO₂NRs. (c) A typical high-resolution TEM (HR-TEM) image of the Pt/TiO₂NRs. The inset shows the magnified image of the region marked by a blue square and (d) size distribution histogram of the PtNPs at the TiO₂NRs surface.

examination of the EDS mapping images can reveal the presence of a few agglomerated PtNPs on the surface of the TiO₂-NRs. The formation of such agglomerated structures might be due to the presence of massive surface defects or oxygen vacancies on the TiO₂NRs surface, which provide active sites for the nucleation and growth of PtNPs.^{40,41} However, the use of NaBH₄, which is a strong reducing agent, makes most of the

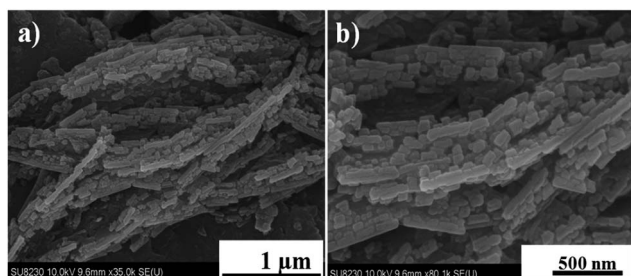


Fig. 1 Typical (a) low, and (b) high-magnification SEM images of as-prepared pristine TiO₂NRs.

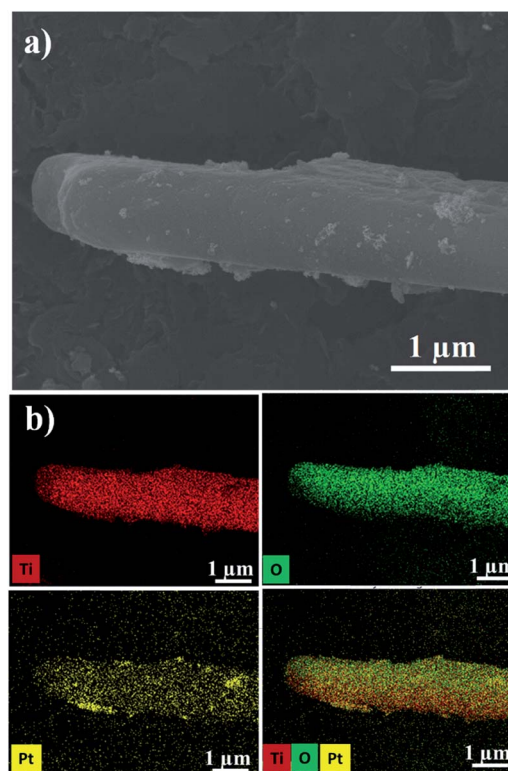


Fig. 3 (a) HAADF-STEM image, (b) the corresponding EDS-elemental mapping images of Ti (red), O (green), Pt (yellow); the overlay image of Pt/TiO₂NRs.

formed PtNPs densely distributed over TiO₂NRs. The densely covered Pt nanoparticles with strong electronic metal–oxide interaction are reported to be very active electrocatalysts, with greatly enhanced performance toward the ORR.²² Furthermore, the EDS spectrum of the composite displayed well-defined emission peaks of Ti, O, and Pt with no other elements, thus providing evidence for the compositional purity of the nanostructures (ESI, Fig. S2†). Through EDS-elemental quantification analysis, the Pt content in the composite was estimated to be about 16.41 wt%.

The structural behaviors of the pristine TiO₂NRs and composite Pt/TiO₂NRs nanostructures were studied by powder X-ray diffraction (XRD) and Raman spectroscopy techniques. Fig. 4a shows the XRD patterns of TiO₂NRs and Pt/TiO₂NRs samples. As can be seen, the pristine TiO₂NRs exhibited diffraction peaks associated with anatase TiO₂ (JCPDS no 23-1078).⁴² For the Pt/TiO₂ sample, in addition to the peaks of TiO₂, four additional diffraction peaks centered at around $2\theta = 39.7, 46.3, 67,$ and 81.5° appeared, which could be assigned to the (111), (220), (220), and (311) planes of metallic Pt in the fcc phase.⁴³ A slight reduction in the intensity of the XRD peaks of TiO₂ was observed due to the incorporation of Pt nanoparticles at the titania surface, which might be due to a mild structural disorder that occurred during the chemical reduction process of Pt ions by the strong reducing agent such as NaBH₄. In addition, Raman spectra were recorded to characterize the Pt/TiO₂-NRs sample (Fig. 4b). The TiO₂NRs exhibited four dispersion bands, all corresponding to the characteristic Raman bands of the anatase TiO₂ nanocrystals.⁴² The peak at 152 cm^{-1} is associated with the O–Ti–O stretching vibration in TiO₂, while in the higher wavenumber region, two low-intensity bands located at $397,$ and 513 cm^{-1} could be associated with the symmetric and antisymmetric bending vibration modes of O–Ti–O, respectively.⁴⁴ For the Pt/TiO₂NRs sample, the intense band at 152 cm^{-1} slightly shifted to higher energy (156 cm^{-1}) and there occurred a slight decrease in the intensity of the band at 640 cm^{-1} compared to its intensity in the TiO₂NRs. These

changes can be ascribed to the presence of strong electronic interactions between PtNPs and TiO₂NRs.²⁰

Fig. 4c displays the UV-vis absorption spectra of the TiO₂NRs and Pt/TiO₂NRs samples. As can be seen, the TiO₂NRs exhibit a strong excitonic absorption peak at 246 nm, with well-defined absorption edge near 350 nm, indicating a small blue shift from the usual band gap energy of TiO₂ (band gap of TiO₂ is approx. 390 nm).⁴⁵ Also, an absorption tail extended to the infrared region, probably arising from the absorption of oxygen vacancies as observed in previous reports.^{46,47} This result indicates that the surface of the as-obtained TiO₂NRs contains oxygen vacancies in high concentration. It is well reported that the surface plasmon resonance (SPR) absorption of small PtNPs (<10 nm) appears below 400 nm. For the Pt/TiO₂NRs sample, the absorption peak of PtNPs was hardly distinguishable because of the intrinsic, strong absorption of the TiO₂, which makes it difficult to observe the SPR peaks of PtNPs.⁴⁸ However, as can be observed, the absorption peak at 246 nm of the TiO₂NRs sample shifted to 269 nm after PtNPs incorporation. Such a large red-shift of the absorption peak of TiO₂NRs on PtNPs incorporation can be ascribed to the change in the dielectric scattering resonance in TiO₂ after the attachment of PtNPs, as was reported in previous study.⁴⁸

The strong electronic interaction between PtNPs and TiO₂-NRs is also evident in the room temperature photoluminescence (PL) spectra of the samples. Fig. 4d displays the PL spectra of the TiO₂NRs and Pt/TiO₂NRs. The TiO₂NRs exhibit strong PL emission at around 361 nm, in addition to three small peaks in the longer wavelength region (400–480 nm). The strong emission band at 361 nm corresponds to the excitonic emission of anatase TiO₂, whereas weak emissions that appeared around 388, 423, and 450 nm are attributed to oxygen vacancy-related defects at the surface of TiO₂NRs.^{41,49} As can be noticed, the overall intensity of the PL emission of the Pt/TiO₂NRs sample is much lower than the emission intensity of TiO₂NRs, especially in the visible region, suggesting a considerable reduction of recombination centers (deep-level) under UV light irradiation, indicating an effective separation and migration of photo-generated charge carriers in the former sample.⁴⁶ It is also worth noting that the weaker peaks that appeared in the 400–800 nm wavelength regions for the TiO₂NRs disappeared after the incorporation of PtNPs. Since these weaker emissions are associated with oxygen vacancy-related defects in TiO₂NRs, which also act as active nucleation centers for PtNPs, the disappearance of these emissions suggests a strong coupling between the formed Pt particles and the TiO₂NRs.

To determine the specific surface area of the fabricated TiO₂NRs and Pt/TiO₂NRs composite samples, their nitrogen (N₂) adsorption–desorption isotherms were recorded at liquid nitrogen temperature (Fig. 5). As can be seen in Fig. 5, the N₂ adsorption–desorption isotherms of both samples reveal hysteresis, characteristic of type IV mesoporous solids. The average pore size in the samples determined using the Barret–Joyner–Halenda (BJH) relation was close to 2.2 nm (inset of Fig. 5). The estimated BET surface area for the TiO₂NRs and Pt/TiO₂NRs were 72 and 80 m² g⁻¹, respectively. The increases in specific surface area and pore size (inset of Fig. 5) on

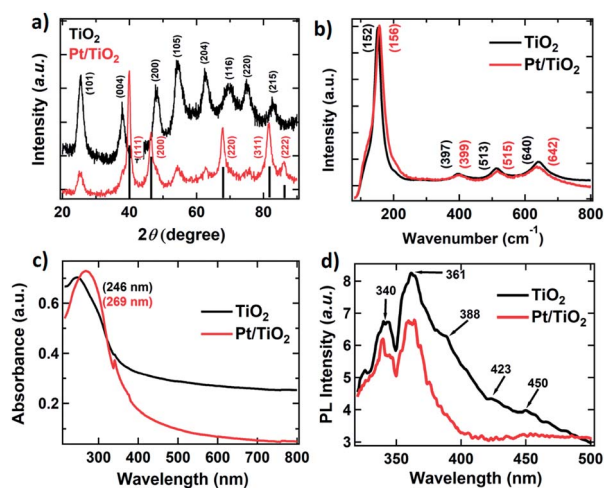


Fig. 4 Structural characterization of the samples: (a) XRD patterns, (b) Raman spectra, (c) UV-vis absorption spectra, and (d) photoluminescence (PL) spectra of pristine TiO₂NRs, and Pt/TiO₂NRs.

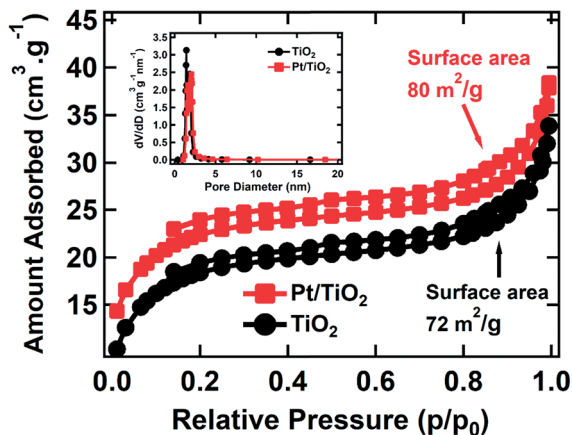


Fig. 5 N_2 adsorption–desorption isotherms of TiO_2 NRs and Pt/ TiO_2 NRs. The inset shows the corresponding pore size distribution plots.

incorporating PtNPs over the TiO_2 NRs are beneficial for the catalytic application of the composite nanostructures.

The surface composition and valence states of elements in the Pt/ TiO_2 NRs sample were analyzed by X-ray photoelectron spectroscopy (XPS). Fig. 6a shows the survey spectra of TiO_2 NRs and Pt/ TiO_2 NRs samples, which contain all the expected emission peaks of TiO_2 , and Pt metallic species at their corresponding specific binding energy positions. The deconvoluted XPS spectrum of the Ti2p region (Fig. 6b) revealed two component bands at binding energy positions 459.1 and 464.92 eV, which could be assigned to the $2p_{3/2}$ and $2p_{1/2}$ emissions of Ti^{4+} , respectively.⁵⁰ In addition, two small shoulder-like peaks at lower BE region, *i.e.* at 458.2 and 464.0 eV, could be assigned to the $2p_{3/2}$ and $2p_{1/2}$ emissions of Ti^{3+} .⁵¹ The core-level O1s spectrum (Fig. 6c) also revealed two components at binding energy positions 530.1 and 531.7 eV, which can be ascribed to the oxygen bonded to titanium (Ti–O), and Pt (Pt–O),

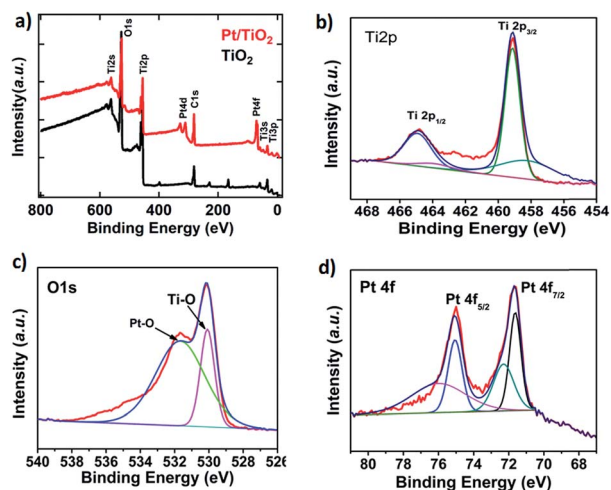


Fig. 6 XPS spectra of the Pt/ TiO_2 NRs composite. (a) XPS survey scan for TiO_2 NRs, and the Pt/ TiO_2 NRs composite. (b–d) High-resolution XPS spectra correspond to the Ti2p (b), O1s (c), and Pt4f (d) emission, respectively.

respectively.⁵² Fig. 6d presents the high-resolution XPS spectrum of the Pt4f emission, revealing Pt4f_{7/2} (71.63 eV) and 4f_{5/2} (74.97 eV) splitting. However, deconvolution of these bands revealed two components each, the binding energies of which correspond to metallic Pt⁰ (71.63 eV for Pt4f_{7/2} and 74.97 eV for Pt4f_{5/2}) and Pt²⁺ (72.31 eV for Pt4f_{7/2} and 75.92 eV for Pt4f_{5/2}).³⁷ The substantially higher intensity of the emission corresponding to Pt in the zero oxidation state (Pt⁰) indicates that most of the Pt incorporated in the sample is in metallic form.⁵³

Electrocatalytic activity of Pt/ TiO_2 NRs towards the ORR

The strong SMSI between metal NPs and oxide supports seem to remarkably enhance their catalytic activity and durability for the oxygen reduction reactions (ORR).^{14,22,53} Thus, the developed Pt/ TiO_2 NRs hybrid structures are expected to act as stable and efficient electrocatalysts for the ORR. The electrocatalytic properties of the Pt/ TiO_2 NRs composite were evaluated after depositing the samples over carbon supports and their activity benchmarked against commercial Pt/C catalyst (20 wt%), and Pt/ TiO_2 (Comm) catalysts. The homogeneous dispersion of the catalysts over carbon support was inspected through their TEM micrographs (ESI, Fig. S3†). Fig. 7a displays the cyclic voltammograms (CVs) of the Pt/ TiO_2 NRs, Pt/ TiO_2 (Comm), and Pt/C catalyst in Ar-saturated 0.1 M $HClO_4$ solution at a scan rate of 20 $mV s^{-1}$ in the potential range -0.2 to 1.0 V vs. Ag/AgCl. The electrochemical surface area (ECA) of the catalysts was derived from the charges associated with the hydrogen adsorption and

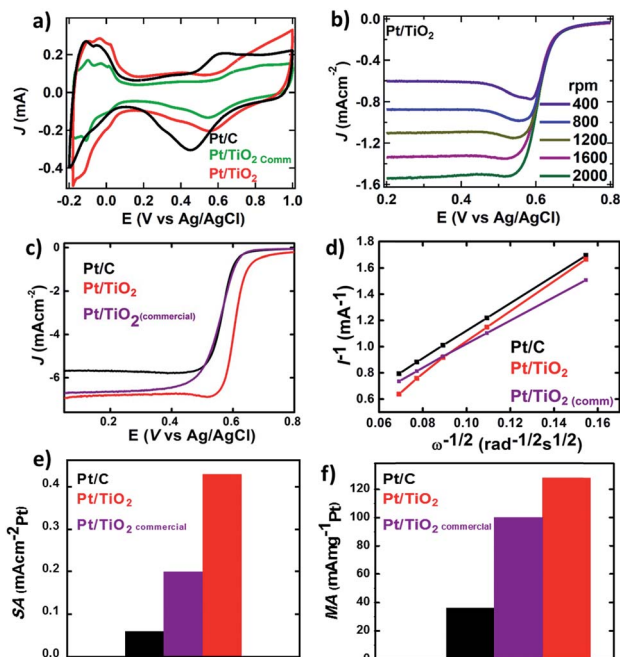


Fig. 7 The electrocatalytic performance of Pt/ TiO_2 NRs catalysts. (a) CV curves of Pt/ TiO_2 NRs, Pt/ TiO_2 (Comm), and Pt/C catalysts; (b) LSV curves of Pt/ TiO_2 NRs at different rotating speeds; (c) LSV curves of the Pt/ TiO_2 NRs, Pt/ TiO_2 (Comm), and Pt/C catalysts in O_2 -saturated 0.1 M $HClO_4$ aqueous solution at 1600 rpm and sweep rate of 2 $mV s^{-1}$. (d) The K–L plots for the catalysts; (e, f) summary of the specific and mass activities of each catalyst at 0.55 V.

desorption regions in the CV curve (Fig. 7a) and normalized by the Pt-loading in the samples.⁵⁴ The estimated ECSA for the Pt/TiO₂NRs, Pt/TiO₂(Comm), and Pt/C catalysts were 64.95, 55.7, and 23.5 m² g⁻¹, respectively (ESI, Fig. S4†). The Pt/TiO₂-NRs catalysts showed a significantly higher ECSA value among the tested catalysts. The higher ECSA for the Pt/TiO₂NRs sample might be due to both the smaller size of the PtNPs (*ca.* 3 nm) and the unique 1D structural features of TiO₂NRs, which can accommodate a larger amount of PtNPs at their surface.

The electrocatalytic activities of the Pt/TiO₂NRs, Pt/TiO₂(Comm), and Pt/C catalysts were further evaluated using the rotating disk electrode (RDE) technique in an O₂-saturated 0.1 M HClO₄ solution at room temperature. The linear sweep voltammetry (LSV) curves with the different rotating speeds of the electrode fabricated with Pt/TiO₂NRs, Pt/TiO₂(Comm), and Pt/C catalysts are shown in Fig. 7b and ESI, Fig. S5.† As can be seen from Fig. 7b, the limiting current increases with the rotation rate of the RDE due to a significant enhancement in mass diffusion at the electrode surface.⁵⁴ Fig. 7c shows the comparison of the LSV curves of the Pt/TiO₂NRs, Pt/TiO₂(Comm), and Pt/C catalysts, collected at the rotation speed of 1600 rpm. As can be seen from Fig. 7c, the Pt/TiO₂NRs catalyst exhibits a half-wave potential at 0.60 V *vs.* Ag/AgCl, which is significantly positively-shifted with respect to those of the Pt/TiO₂(Comm) (0.563 V), and Pt/C catalyst (0.56 V). Such a high positive shift in the half-wave potential value for the strongly coupled Pt/TiO₂-NRs catalyst suggests their enhanced ORR electrocatalytic activity.

To understand the electron transfer kinetics of the ORR in detail, the number of transferred electrons was calculated using the Koutecky–Levich (K–L) equation. The K–L plots for the Pt/TiO₂NRs, Pt/TiO₂(Comm), Pt/C catalysts derived from the LSV curves are presented in Fig. 7d. The K–L plots exhibit the good linear dependence of the inverse limiting current on the inverse square root of rotation frequency (ω) (Fig. 7d), indicating first-order reaction kinetics against the dissolved oxygen on the surface of the electrode. From the slopes of the K–L plots, the exact number of transferred electrons (*n*) was calculated. The estimated *n*-value is four, suggesting a stable, four-electron-pathway for the ORR. The Tafel plots of the Pt/TiO₂NRs, Pt/TiO₂(Comm), and Pt/C catalysts are shown in ESI, Fig. S6.† The Tafel slopes for Pt/TiO₂NRs, Pt/TiO₂(Comm), and Pt/C catalysts in the kinetic and mixed kinetic-diffusion controlled regions (0.5 V < *E*) were 90 mV dec⁻¹, 91 mV dec⁻¹ and 92 mV dec⁻¹, respectively. The low Tafel slope value of the Pt/TiO₂NRs catalyst indicates its excellent kinetic performance in the ORR. The possible ORR reaction mechanism in the Pt/TiO₂NRs hybrid catalyst could be the pristine TiO₂NRs containing oxygen vacancies at high concentration at their surface, which facilitate the incorporation of PtNPs at their surface through SMSI. In comparison to Pt deposited on the oxygen sites, the PtNPs supported on the oxygen vacancy sites are more electronegative and possess few –OH functional groups at their surface in the ORR,¹⁴ which serve as active sites and improve the electron transfer rate at the functional interface of the PtNPs/TiO₂NRs hybrid nanostructure.

To further evaluate the performance of the catalysts, we calculated the specific activities (SA) and mass activities (MA) of

Pt/TiO₂NRs and compared them with the same for the Pt/TiO₂(Comm), and Pt/C catalysts (Fig. 7e, f). As can be seen in Fig. 7e, the Pt/TiO₂NRs exhibits a SA value of 0.428 mA cm⁻² at 0.55 V *vs.* Ag/AgCl, which is 2.2 and 7.2 times higher than the state-of-the-art Pt/TiO₂(Comm) (0.198 mA cm⁻²), and Pt/C (0.059 mA cm⁻²) catalysts, respectively. Under the same potential, the mass activity of Pt/TiO₂NRs was calculated to be 128 mA mg_{Pt}⁻¹ (Fig. 7f), which is 3.5 times higher than the MA of the Pt/C catalyst (36 mA mg_{Pt}⁻¹) and 1.28 times greater than the MA of the Pt/TiO₂(Comm) (99.76 mA mg_{Pt}⁻¹) catalyst. In addition, the SA and MA activity of the catalysts were also calculated at 0.9 V (*vs.* rotating hydrogen electrode (RHE)) and the values are shown in Table S1.† The electrocatalytic activity of the Pt/TiO₂NRs catalyst is higher in comparison with the previously reported PtNPs supported catalysts (Table S1†).^{11,50,54–57} Even though the ECSA of our Pt/TiO₂NRs catalyst is slightly lower as compared to other reported catalysts, it exhibits significantly higher specific and mass activities, clearly demonstrating the superior electrocatalytic performance of the hybrid Pt/TiO₂NRs catalyst fabricated in the present work. The greatly enhanced catalytic performance of the Pt/TiO₂NRs catalyst can be attributed to the strongly coupled smaller PtNPs over TiO₂NRs. This was indirectly confirmed by different characterization techniques that facilitate electron transfer across the interfaces, as well as the unique 1D feature of the TiO₂NRs that provides a higher surface area, which permits the uniform dispersion of PtNPs and multipoint interactions with the carbon support. To verify the presence of strong metal-support interactions in the fabricated Pt/TiO₂NRs catalyst, we further performed CO-stripping measurements on all the catalysts. The CO-stripping curves for Pt/TiO₂NRs, Pt/TiO₂(Comm), and Pt/C catalysts have been presented in the ESI Fig. S7.† As can be seen in Fig. S7,† the CO oxidation peak potential for the as-synthesized Pt/TiO₂NRs suffered a significant negative shift in comparison to the CO-oxidation potential of the Pt/TiO₂(Comm), and Pt/C catalysts. The large shift in the CO oxidation peak towards negative potential suggests a strong coupling of PtNPs with the TiO₂NRs support. The obtained results clearly indicate that the present synthesis approach provides several advantages over other chemical synthetic routes such as facile and environmentally friendly synthesis on the bulk scale, excellent control over the morphology, higher surface area and improved ORR activity, characteristics that are highly desirable for the development of highly efficient electrocatalysts for fuel cell applications.

The durability of the Pt/TiO₂NRs catalysts

It is well reported that the detachment of the supported NPs can severely affect the stability of the supported electrocatalysts under harsh fuel-cell operation conditions.⁷ Thus, the electrochemical durability of the Pt/TiO₂NRs catalyst was assessed using accelerated durability tests (ADTs) through 10 000 repeated scanning cycles in Ar-saturated 0.1 M HClO₄ solution at the applied potential range of +0.5 to +1.0 V (*vs.* Ag/AgCl), and the results were compared with the Pt/C, Pt/TiO₂(Comm) catalyst. Fig. 8a compares the CV curves of Pt/TiO₂NRs, Pt/TiO₂(Comm), and Pt/C catalysts before and after 10 000 sweeping

cycles. As can be seen from Fig. 8a, the CVs of the Pt/TiO₂NRs catalyst before and after ADTs almost overlapped, while the current densities (j) of the Pt/TiO₂(Comm) and Pt/C catalysts after ADTs significantly decreased. Fig. 8b shows the ORR polarization curves before and after ADTs for the Pt/TiO₂NRs, Pt/TiO₂(Comm), and Pt/C catalysts. It is evident that after 10 000 sweeping cycles, the ORR polarization curve of the Pt/TiO₂NRs catalyst suffered only a negligible shift. In contrast, for the Pt/TiO₂(Comm) and Pt/C catalysts, the ORR polarization curve suffered a significant shift. In particular, the half-wave reduction potential of Pt/TiO₂NRs decreased slightly from 0.67 to 0.62, whereas for the Pt/TiO₂(Comm) and Pt/C catalysts, the decrease in reduction potential was significant (from 0.63 to 0.56 V for Pt/TiO₂(Comm), and from 0.64 to 0.51 V for Pt/C) after 10 000 cycles. In addition, the ECSA was degraded by only about 36% for the Pt/TiO₂NRs catalyst, while the same for the Pt/TiO₂(Comm) and Pt/C catalysts were decreased by 57% and 65% of their initial values (Fig. 8c). The obtained results clearly indicate the superior stability of the as-prepared Pt/TiO₂NRs catalyst. Previous studies have revealed that the stability of composite electrocatalysts suffers a drastic reduction in ECSA due to the degradation and detachment of metal NPs from the support surface, and the interdiffusion of metal atoms *via* Ostwald ripening during their electrochemical operations.² The superior stability of our as-obtained Pt/TiO₂NRs catalyst could be due to the unique 1-D structure of TiO₂NRs, the presence of multipoint contacts with the carbon support through well-dispersed small PtNPs, as well as strong coupling between the PtNPs and TiO₂NRs. The strong binding of PtNPs not only suppresses their aggregation/agglomeration but also prevents their detachment and migration over the TiO₂NRs support during electrocatalytic measurements. To evaluate the changes suffered by the PtNPs during their electrochemical tests, we performed TEM studies on the Pt/TiO₂NRs and Pt/C catalysts after their ADTs (Fig. 8d and ESI, Fig. S8†). Fig. 8d displays a typical TEM image of the catalysts after ADTs, which revealed

that most of the PtNPs remained well dispersed over TiO₂NRs, without their significant aggregation or change in morphology. However, the ADTs apparently affect the crystalline nature of the TiO₂NRs. To demonstrate the change in the interaction between PtNPs and TiO₂NRs after ADT, XPS analysis of the composite nanostructures was carried out after their utilization (ESI, Fig. S9†). The binding energy positions of Ti2p, O1s, and Pt4f emissions suffered only a small shift toward lower BE values after ADT, further indicating the presence of strong interactions between PtNPs and TiO₂NRs in the Pt/TiO₂NRs hybrid nanocomposite. Overall, these results provide strong evidence of SMSI and demonstrate that the smaller PtNPs over 1D TiO₂NRs in the hybrid Pt/TiO₂NRs nanostructure facilitate the electrically favorable functional interface for achieving enhanced electrocatalytic activity for the ORR.

Conclusions

We have demonstrated a novel macroalgae polymer-mediated approach for the fabrication of TiO₂NRs and the Pt/TiO₂NRs hybrid nanostructure using a green method. The smaller size of the PtNPs (*ca.* 3 nm) and high density of surface defects/oxygen vacancies facilitated the strong coupling of PtNPs at the surface of the TiO₂NRs. The resultant hybrid Pt/TiO₂NRs catalyst exhibited greatly enhanced electrocatalytic activity toward the ORR in comparison to the Pt/TiO₂(Comm), Pt/C catalysts. Moreover, the fabricated Pt/TiO₂NRs catalyst demonstrated its high stability even after 10 000 potential sweeping cycles in the ORR. Detailed structural characterization of the composite revealed the existence of strong electronic interactions between PtNPs and the TiO₂NRs support. The improved performance of the Pt/TiO₂NRs catalyst can be ascribed to the oxygen vacancy-mediated strong coupling between the metal and metal oxide components and the unique 1D structure of TiO₂NRs, which enhanced the electron transfer rate at the metal–semiconductor interface. Moreover, the linear morphology of the TiO₂NRs facilitated the directional (structure-mediated) charge transport, enhancing the conductivity of the active electrode fabricated using the Pt/TiO₂NRs composite. The present approach to the controlled growth of TiO₂NRs and fabrication of hybrid Pt/TiO₂NRs nanostructures provides not only a novel, green, and cost-effective protocol for the fabrication of metal–metal oxide nanocomposites with controlled morphology and dimensions, but also provides nanostructured electrocatalysts with enhanced activities that are in high demand for fuel cell applications.

Conflicts of interest

There are no conflicts to declare.

Acknowledgements

SKK acknowledges CONACyT, Mexico, for offering the Cathedra position (Project No. 649). Authors also thank NIMS-Japan for providing materials characterization support.

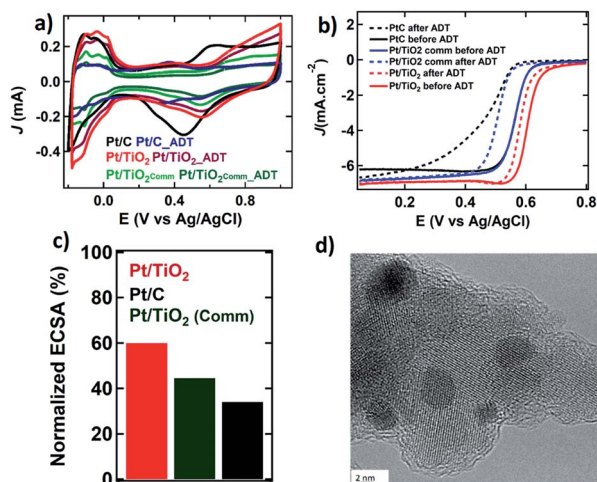


Fig. 8 (a) CVs of Pt/TiO₂NRs, Pt/TiO₂(Comm), and Pt/C catalysts before and after ADTs. (b) LSV curves of the three different catalysts in O₂-saturated 0.1 M HClO₄ before and after 10 000 sweeping cycles in the durability test. (c) A comparison of the ECSA of each catalyst after ADTs; (d) a typical TEM image of the Pt/TiO₂NRs after the durability test.

Notes and references

- 1 M. K. Debe, *Nature*, 2012, **486**, 43–51.
- 2 M. Li, M. Li, Z. Zhao, T. Cheng, A. Fortunelli, C. Chen, R. Yu, L. Gu, B. Merinov, Z. Lin, E. Zhu, T. Yu, Q. Jia, J. Guo, L. Zhang, W. a G. Iii, Y. Huang and X. Duan, *Science*, 2016, **354**, 1414–1419.
- 3 H. Mistry, A. S. Varela, S. Kühl, P. Strasser and B. R. Cuenya, *Nat. Rev. Mater.*, 2016, 1–14.
- 4 D. Banham and S. Ye, *ACS Energy Lett.*, 2017, **2**, 629–638.
- 5 W. Yu, M. D. Porosoff and J. G. Chen, *Chem. Rev.*, 2012, **112**, 5780–5817.
- 6 Y. Xia and X. Yang, *Acc. Chem. Res.*, 2017, **50**, 450–454.
- 7 C. Ray and T. Pal, *J. Mater. Chem. A*, 2017, **5**, 9465–9487.
- 8 G. N. Vayssilov, Y. Lykhach, A. Migani, T. Staudt, G. P. Petrova, N. Tsud, T. Skála, A. Bruix, F. Illas, K. C. Prince, V. Matolín, K. M. Neyman and J. Libuda, *Nat. Mater.*, 2011, **10**, 310–315.
- 9 C. Jackson, G. T. Smith, D. W. Inwood, A. S. Leach, P. S. Whalley, M. Callisti, T. Polcar, A. E. Russell, P. Levecque and D. Kramer, *Nat. Commun.*, 2017, **8**, 1–11.
- 10 K. Jukk, N. Kongi, K. Tammeveski, R. M. Arán-Ais, J. Solla-Gullón and J. M. Feliu, *Electrochim. Acta*, 2017, **251**, 155–166.
- 11 B. J. Hsieh, M. C. Tsai, C. J. Pan, W. N. Su, J. Rick, H. L. Chou, J. F. Lee and B. J. Hwang, *Electrochim. Acta*, 2017, **224**, 452–459.
- 12 Z. Weng, W. Liu, L. C. Yin, R. Fang, M. Li, E. I. Altman, Q. Fan, F. Li, H. M. Cheng and H. Wang, *Nano Lett.*, 2015, **15**, 7704–7710.
- 13 B.-J. Hsieh, M.-C. Tsai, C.-J. Pan, W.-N. Su, J. Rick, J.-F. Lee, Y.-W. Yang and B.-J. Hwang, *NPG Asia Mater.*, 2017, **9**, 1–8.
- 14 K. Tammeveski, T. Tenno, A. Rosental, P. Talonen, L. Johansson and L. Niinistö, *J. Electrochem. Soc.*, 1999, **146**, 669–676.
- 15 V. T. T. Ho, C. Pan, J. Rick, W. Su and B. Hwang, *J. Am. Chem. Soc.*, 2011, **133**, 11716–11724.
- 16 A. Ostroverkh, V. Joha, P. Ku and S. Romana, *Langmuir*, 2016, **32**, 6297–6309.
- 17 H. Xu, A. Wang, Y. Tong and G. Li, *ACS Catal.*, 2016, **6**, 5198–5206.
- 18 K. An, Q. Zhang, S. Alayoglu, N. Musselwhite, J. Y. Shin and G. a. Somorjai, *Nano Lett.*, 2014, **14**, 4907–4912.
- 19 S. K. Meher and G. R. Rao, *J. Phys. Chem. C*, 2013, **117**, 4888–4900.
- 20 Z. Xi, D. P. Erdosy, A. Mendoza-garcia, P. N. Duchesne, J. Li, M. Muzzio, Q. Li, P. Zhang and S. Sun, *Nano Lett.*, 2017, **17**, 2727–2731.
- 21 M. Liu, W. Tang, Z. Xie, H. Yu, H. Yin, Y. Xu, S. Zhao and S. Zhou, *ACS Catal.*, 2017, **7**, 1583–1591.
- 22 Q. Jia, S. Ghoshal, J. Li, W. Liang, G. Meng, H. Che, S. Zhang and S. Mukerjee, *J. Am. Chem. Soc.*, 2017, **139**, 7893–7903.
- 23 H. Hussain, G. Tocci, T. Woolcot, X. Torrelles, C. L. Pang, D. S. Humphrey, C. M. Yim, D. C. Grinter, G. Cabailh, O. Bikondoa, R. Lindsay, J. Zegenhagen, A. Michaelides and G. Thornton, *Nat. Mater.*, 2017, **16**, 461–467.
- 24 A. L. Linsebigler, G. Lu and J. T. Yates, *Chem. Rev.*, 1995, **95**, 735–758.
- 25 S. Jin, C. Li, L. K. Shrestha, Y. Yamauchi, K. Ariga and J. P. Hill, *ACS Appl. Mater. Interfaces*, 2017, **9**, 18782–18789.
- 26 M. C. Groenenboom, R. M. Anderson, D. J. Horton, Y. Basdogan, D. F. Roeper, S. A. Policastro and J. A. Keith, *J. Phys. Chem. C*, 2017, **121**, 16825–16830.
- 27 X. Wang, Z. Li, J. Shi and Y. Yu, *Chem. Rev.*, 2014, **114**, 9346–9384.
- 28 J. Chen, H. Bin Yang, J. Miao, H. Wang and B. Liu, *J. Am. Chem. Soc.*, 2014, **136**, 15310–15318.
- 29 J. Joo, S. G. Kwon, T. Yu, M. Cho, J. Lee, J. Yoon and T. Hyeon, *J. Phys. Chem. B*, 2005, **109**, 15297–15302.
- 30 M. Yang, B. Ding, S. Lee and J.-K. Lee, *J. Phys. Chem. C*, 2011, **115**, 14534–14541.
- 31 L. K. Dhandole, M. A. Mahadik, S.-G. Kim, H.-S. Chung, Y.-S. Seo, M. Cho, J. Ryu and J. S. Jang, *ACS Appl. Mater. Interfaces*, 2017, **9**, 23602–23613.
- 32 J. C. Colmenares, R. S. Varma and P. Lisowski, *Green Chem.*, 2016, **18**, 5736–5750.
- 33 S. Rajeshkumar, C. Malarkodi, G. Gnanajobitha and K. Paulkumar, *J. Nanostruct. Chem.*, 2013, **3**, 1–7.
- 34 P. D. Shankar, S. Shobana, I. Karuppusamy, A. Pugazhendhi, V. S. Ramkumar, S. Arvindnarayan and G. Kumar, *Enzyme Microb. Technol.*, 2016, **95**, 28–44.
- 35 H. A. Gasteiger, S. S. Kocha, B. Sompalli and F. T. Wagner, *Appl. Catal., B*, 2005, **56**, 9–35.
- 36 Y. Yin and A. P. Alivisatos, *Nature*, 2005, **437**, 664–670.
- 37 P. S. Murphin Kumar, S. Thiripuranthagan, T. Imai, G. Kumar, A. Pugazhendhi, S. K. Vijayan, R. Esparza, H. Abe and S. K. Krishnan, *ACS Sustainable Chem. Eng.*, 2017, **5**, 11290–11299.
- 38 S. Heo, J. Kim, G. K. Ong and D. J. Milliron, *Nano Lett.*, 2017, **17**, 5756–5761.
- 39 F. Shi, L. R. Baker, A. Hervier, G. A. Somorjai and K. Komvopoulos, *Nano Lett.*, 2013, **13**, 4469–4474.
- 40 X. Pan and Y. J. Xu, *J. Phys. Chem. C*, 2013, **117**, 17996–18005.
- 41 Y. Lu, Y. Jiang, X. Gao, X. Wang and W. Chen, *J. Am. Chem. Soc.*, 2014, **136**, 11687–11697.
- 42 L. De Trizio, R. Buonsanti, A. M. Schimpf, A. Llordes, D. R. Gamelin, R. Simonutti and D. J. Milliron, *Chem. Mater.*, 2013, **25**, 3383–3390.
- 43 Y. Fan, Z. Yang, P. Huang, X. Zhang and Y. M. Liu, *Electrochim. Acta*, 2013, **105**, 157–161.
- 44 F. Tian, Y. Zhang, J. Zhang and C. Pan, *J. Phys. Chem. C*, 2012, **116**, 7515–7519.
- 45 M. D. Driessen and V. H. Grassian, *J. Phys. Chem. B*, 1998, **5647**, 1418–1423.
- 46 H. Song, C. Li, Z. Lou, Z. Ye and L. Zhu, *ACS Sustainable Chem. Eng.*, 2017, **5**, 8982–8987.
- 47 W. K. Wang, J. J. Chen, W. W. Li, D. N. Pei, X. Zhang and H. Q. Yu, *ACS Appl. Mater. Interfaces*, 2015, **7**, 20349–20359.
- 48 N. Zhang, C. Han, Y. Xu, J. J. F. Iv, D. Zhang, J. Codrington, S. K. Gray and Y. Sun, *Nat. Photonics*, 2016, **10**, 473–483.
- 49 J. Yu, L. Qi and M. Jaroniec, *J. Phys. Chem. C*, 2010, **114**, 13118–13125.

- 50 J. Li, H. Zhou, H. Zhuo, Z. Wei, G. Zhuang, X. Zhong, S. Deng, X. Li and J. Wang, *J. Mater. Chem. A*, 2018, **6**, 2264–2272.
- 51 R. Boppella, J.-E. Lee, F. M. Mota, J. Y. Kim, Z. Feng and D. H. Kim, *J. Mater. Chem. A*, 2017, **5**, 7072–7080.
- 52 M. Imran, A. B. Yousaf, X. Zhou, Y. F. Jiang, C. Z. Yuan, A. Zeb, N. Jiang and A. W. Xu, *J. Phys. Chem. C*, 2017, **121**, 1162–1170.
- 53 A. Bin Yousaf, M. Imran, N. Uwitonze, A. Zeb, S. J. Zaidi, T. M. Ansari, G. Yasmeen and S. Manzoor, *J. Phys. Chem. C*, 2017, **121**, 2069–2079.
- 54 K. R. Deepthi, G. V. Ramesh, R. Kodyath, P. S. Murphin Kumar, A. Dakshanamoorthy and H. Abe, *J. Mater. Chem. A*, 2017, **5**, 1667–1671.
- 55 A. Zana, C. Rüdiger, J. Kunze-Liebhäuser, G. Granozzi, N. E. A. Reeler, T. Vosch, J. J. K. Kirkensgaard and M. Arenz, *Electrochim. Acta*, 2014, **139**, 21–28.
- 56 L. Guo, W. J. Jiang, Y. Zhang, J. S. Hu, Z. D. Wei and L. J. Wan, *ACS Catal.*, 2015, **5**, 2903–2909.
- 57 S.-Y. Huang, P. Ganesan and B. N. Popov, *ACS Catal.*, 2012, **2**, 825–831.